

Baseline-dependent sampling and windowing for radio interferometry: data compression, field-of-interest shaping and outer field suppression

M. Atemkeng^{1*}, O. Smirnov^{1,2}, C. Tasse^{1,3}, G. Foster^{4,5}, A. Keimpema⁶,
Z. Paragi⁶ and J. Jonas^{1,2}

¹*Department of Physics and Electronics, Rhodes University, PO Box 94, Grahamstown, 6140, South Africa*

²*SKA South Africa, 3rd Floor, The Park, Park Road, Pinelands, 7405, South Africa*

³*GEPI, Observatoire de Paris, CNRS, Universite Paris Diderot, 5 place Jules Janssen, 92190 Meudon, France*

⁴*University of Oxford, Sub-Department of Astrophysics, Denys Wilkinson Building, Keble Road, Oxford, OX1 3RH, UK*

⁵*Department of Astronomy, University of California, Berkeley, 501 Campbell Hall #3411, Berkeley, CA, 94720, USA*

⁶*Joint Institute for VLBI ERIC in Europe, Oude Hoogeveensedijk 4, 7991 PD Dwingeloo, Netherlands*

Accepted 2018 March 02. Received 2018 February 07; in original form 2017 October 07

ABSTRACT

Traditional radio interferometric correlators produce regular-gridded samples of the true uv -distribution by averaging the signal over constant, discrete time-frequency intervals. This regular sampling and averaging then translate to be irregular-gridded samples in the uv -space, and results in a baseline-length-dependent loss of amplitude and phase coherence, which is dependent on the distance from the image phase centre. The effect is often referred to as “decorrelation” in the uv -space, which is equivalent in the source domain to “smearing”. This work discusses and implements a regular-gridded sampling scheme in the uv -space (baseline-dependent sampling) and windowing that allow for data compression, field-of-interest shaping and source suppression. The baseline-dependent sampling requires irregular-gridded sampling in the time-frequency space i.e. the time-frequency interval becomes baseline-dependent. Analytic models and simulations are used to show that decorrelation remains constant across all the baselines when applying baseline-dependent sampling and windowing. Simulations using MeerKAT telescope and the European Very Long Baseline Interferometry Network show that both data compression, field-of-interest shaping and outer field-of-interest suppression are achieved.

Key words: Instrumentation: interferometers, Methods: data analysis, Methods: numerical, Techniques: interferometric

1 Introduction and motivations

A variety of new radio telescopes, precursors (e.g. ASKAP (Johnston et al. 2008), MeerKAT (Jonas 2009)) and Pathfinders (e.g. LOFAR (Van Haarlem et al. 2013), NenuFAR (Zarka et al. 2015)) for the Square Kilometre Array (Dewdney et al. 2009) (SKA) are under development or used to image wide field of view (FoV, i.e. the fractional portion of the primary beam at the full width at half maximum (FWHM)) sky surveys at high sensitivity, wide bandwidth and high spectral and temporal resolution. These radio telescopes produce an extremely large volume of data, such that data storage and analysis are becoming more challenging for scientific research and engineering requirements e.g., to

transmit the data from the receivers to the correlator or in data reduction such as calibration and imaging. A typical example is the LOFAR telescope. Its uv -data (visibilities), assuming 24 core stations (excluding the remote and international stations) using 244 sub-bands with 64 channels per sub-band, 4 hours observation time with a 1 s temporal resolution is predicted to be ~ 8376 GB using the dual high band antenna (see LOFAR calculator¹). However, observations with all the LOFAR national and international stations are capable of producing data volumes of the order of petabytes (Sabater et al. 2017). Survey capabilities with the future SKA (unprecedented sensitivity, resolution and

* E-mail: m.atemkeng@gmail.com

¹ lofar.astron.nl/service/pages/storageCalculator/calculate.jsp

bandwidth) are expected to generate data by many orders of magnitude higher than any existing radio interferometer. This data volume will be even larger for any SKA survey science that will integrate multiple beams and/or multiple phase tracking e.g., African Very Long Baseline Interferometry (VLBI) Network (Gaylard et al. 2014), European VLBI Network (EVN) (Keimpema et al. 2015), etc. New techniques for data compression and storage systems must be developed for the transition from the current radio interferometers to the SKA. Data compression is an advantageous solution for increasing the speed of the data transmission and to decrease the computational requirements for post-processing. Data compression also offers an alternative possibility for wide FoV observations because it offers significant reduction of the data volume while preserving useful information to improve discovery and analysis accuracy.

Traditionally, radio interferometric correlators compress the visibility data by simply averaging the data, which may be averaged further in post-correlation to speed up processing. However, the challenge in compressing the visibilities by simple averaging is that these visibilities decorrelate and the decorrelation is time-frequency dependent and baseline-dependent. The visibility from a baseline pq (with vector $\mathbf{u}_{pq} = (u, v, w)$) of a point source with brightness S and coordinates $\mathbf{l} = (l, m, n - 1)$ is given by:

$$V_{pq} = S \exp \{ -i\phi \}, \quad \phi(\mathbf{u}_{pq}) = 2\pi \mathbf{u}_{pq} \cdot \mathbf{l}. \quad (1)$$

For sources with an increasing separation from the phase centre, the phase ϕ is increasingly large for a given baseline, and at some distance phase-wrapping within the averaging time-frequency will cause a strong decorrelation of the signal. Figure 1 is a simulated observation with MeerKAT at 1.4 GHz showing the amplitude decorrelation for a 1 Jy point source located at 0.65 deg, 1.32 deg and 2.25 deg away from the phase tracking centre as a function of East-West baseline length. At this frequency, a MeerKAT survey must be able to image sources up to an angular distance of 0.65 deg (edge of the FoV at the FWHM of the primary beam (PB)) from the phase tracking centre with little to no smearing effects. But modern calibration and imaging techniques such as MeqTrees (Noordam & Smirnov 2010) or DDFacet (Tasse et al. 2017) are able to correct for PB effects far exceed the second sidelobe of the PB (Mitra et al. 2015). An accurate PB model is necessary for calibrating out the effects of the PB, and for improving image fidelity. A good PB model can significantly reduce artefacts in the image and improve its dynamic range, and an appropriate direction-dependent calibration procedure can further reduce artefacts and increase the dynamic range (Mitra et al. 2015). Throughout this paper, we use the term Field-of-Interest (FoI) to differentiate from the FoV when the region of interest to be imaged exceed “the fractional portion of the PB at the FWHM”. The first and the second null of the PB of MeerKAT at 1.4 GHz fall at ~ 1.32 and ~ 2.25 deg respectively. In Figure 1 the pre-averaged data is simulated using 1 s and 84 kHz for time and frequency resolutions respectively. To evaluate the time smearing the data is simple averaged across 15 s and the frequency resolution remains fixed to 84 kHz. Similarly, for the bandwidth smearing the time resolution is maintains to 1 s and the data is simple averaged across 0.84 MHz in frequency. Results show that decorrelation/smearing is severe on longer East-West baselines than shorter East-West

baselines and that smearing is a function of source position in the sky.

Simple averaging could be used in a way to increase the signal-to-noise ratio (SNR) within the FoI by suppressing the sidelobes from sources out of the FoI, but the drawback is that sources at the edges of the FoI will be smeared (Lonsdale et al. 2004; Atemkeng et al. 2016). However, increasing the SNR based on averaging is feasible only if both the FoI and its edges are preserved from smearing, and sources out of the FoI are suppressed. The later is resumed mathematically as follows:

$$\text{SNR} \approx \frac{S_{\text{smear}}}{C_{\text{noise}} + T_{\text{noise}}}, \quad (2)$$

where S_{smear} is the signal of a source in the FoI (including the edges) that must be preserved from smearing, C_{noise} the signal from sources outside the FoI (i.e. confusion noise) that must be subtracted from the FoI or must strongly decorrelate and T_{noise} the thermal noise which is usually Gaussian and intrinsic to the visibility measurement process. Ideally, one wants an increase in S_{smear} and a decrease in C_{noise} within the FoI, so that the overall SNR increased even if there is an increase in T_{noise} in the case of weighted averaging.

If the uv -coverage of an interferometer is condensed at the centre then most of the data comes from the shorter baselines. An example of this type of centrally condensed uv -coverage along with the uv -coverage histogram is illustrated in Figure 2. The histogram shows the uv -coverage data density as a function of effective baseline length. If more samples should be averaged at the centre and fewer at the outer, decorrelation can be avoided on the longer baselines and data compression would be carried out on the shorter baselines. This method, often referred to as baseline-dependent averaging (BDA), was first proposed by Cotton (1989, 1999) as an approach for dealing with wide field imaging with little to no bandwidth and time averaging effects.

The idea of BDA is thus not novel, and has also been subject of discussion in many radio interferometry conferences, particularly the ability to use BDA for the SKA data processors. Atemkeng et al. (2016) discussed a baseline-dependent window functions (BDWFs) scheme that has the effect to shape the FoI. Several other techniques to shape the FoI using window functions have been proposed (Lonsdale et al. 2004; Parsons & Backer 2009; Parsons et al. 2016). BDWFs are weighted-moving averaging of the irregular sampled visibilities in the uv -space. The mathematical derivations for the BDWFs show that the dirty image is the apparent sky multiplied by the inverse Fourier transform of each of the BDWFs. This work removes the restriction of irregular sampling in uv -space adopted in Atemkeng et al. (2016) and considers regular sampling and averaging in the uv -space as a BDA formalism. To shape the FoI, the BDA formalism is applied to BDWFs, i.e. applying weighted-moving averaging to the regular sampled visibilities in the uv -space. Throughout this paper, we will be referring BDA applied to BDWFs as BDAWFs. Since an unweighted average represents theoretically maximum sensitivity at the centre of the FoI, a weighted averaging will result in a loss in nominal sensitivity. However, to alleviate the decrease in sensitivity, BDWFs are further extended by Atemkeng et al. (2016), showing that

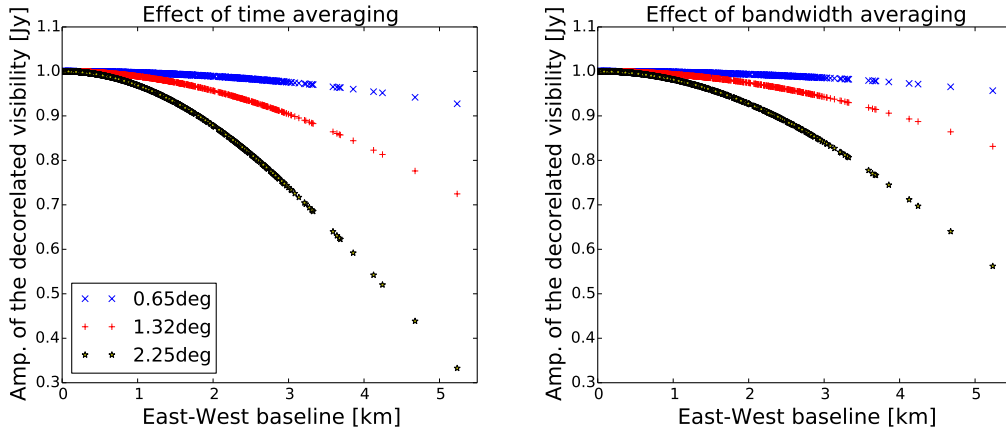


Figure 1. Amplitude loss: the apparent intensity of a 1 Jy source at 0.65 deg, 1.32 deg and 2.25 deg as seen by MeerKAT at 1.4 GHz as a function of East-West baseline components; (Left): data is simple averaged across 15 s in time and frequency resolution is fixed to 84 kHz; (Right) data is simple averaged across 0.84 MHz in frequency and time resolution is fixed to 1 s.

the use of overlapping BDWFs has the benefit of suppressing the far FoI sources compared to simple averaging, and could even recover some of the lost sensitivity while decreasing the overall far-field confusion noise. Overlapping BDWFs are sets of polyphase finite impulse response filters with order depending on the overlapping bins in the uv -space. The overlapping bins compensate for the missing bins windowed with the BDWF. We refer the reader to Atemkeng et al. (2016) for an intensive discussion on BDWFs and properties of overlapping BDWFs. The mathematical framework derived from the BDAWFs formalism shows that the dirty image is the apparent sky multiplied by the inverse Fourier transform of a single BDWF.

2 Mathematical background

We use the radio interferometry measurement equation (RIME) formalism, which provides a model of a generic interferometer. For details on the RIME formalism see Hamaker et al. (1996); Smirnov (2011a,b). In a single mathematical equation, the RIME describes all the direction-dependent and direction-independent effects that may occur when an interferometric measurement is in process. The 2-D Fourier transform full sky RIME, following Smirnov (2011a,b), is given by:

$$\mathcal{V}_{pq} = \mathbf{G}_{pt\nu} \left(\iint_{lm} \mathbf{D}_{pt\nu} \mathcal{I} \mathbf{D}_{qt\nu}^H e^{-i\phi} dl dm \right) \mathbf{G}_{qt\nu}^H, \quad (3)$$

where the superscript $(.)^H$ denotes a Hermitian transpose operator. Here a single visibility value is denoted by V_{pq} or in functional form by $\mathcal{V}_{pq} \equiv \mathcal{V}(\mathbf{u}_{pq})$ and the sky distribution function by $\mathcal{I} \equiv \mathcal{I}(l, m)$. The formalism groups the product of direction-independent Jones matrices corresponding to antenna p into the matrix $\mathbf{G}_{pt\nu}$, and all its direction-dependent effects into the matrix $\mathbf{D}_{pt\nu}$. We note that the PB pattern of each of the antenna that defines the directional sensitivity and the FoV of each of the antennas is part of the direction-dependent effects. The term $\mathbf{D}_{pt\nu} \mathcal{I} \mathbf{D}_{qt\nu}^H$ is the apparent sky seen by baseline pq , and varies in time and frequency. For simplicity, throughout this work we assume that

both the sky and the direction-dependent gain are invariant; therefore each of the baselines will see the same apparent sky throughout the measurement process.

Rotation of the Earth causes the baseline phase to vary in time, and for multi-frequency observations the phase is constantly changing with time and frequency. In practical situations an interferometer can only measure an average visibility over a fixed time-frequency lengths as given by the *sampling bin*:

$$\mathbf{B}_{kr}^{[\Delta t \Delta \nu]} = \left[t_k - \frac{\Delta t}{2}, t_k + \frac{\Delta t}{2} \right] \times \left[\nu_r - \frac{\Delta \nu}{2}, \nu_r + \frac{\Delta \nu}{2} \right], \quad (4)$$

where Δt centered at t_k and $\Delta \nu$ centred at ν_r are the sampling intervals in time and frequency respectively. The sampling bin has two dimensions: the width and height measured in time and frequency respectively. Let us denote $\mathcal{V}_{pq}(\mathbf{u}(t, \nu)) \equiv \mathcal{V}(\mathbf{u}_{pq}(t, \nu))$ as the ideal visibility distribution. After averaging in the correlator, the measured visibility becomes:

$$\tilde{\mathcal{V}}_{pqkr} = \frac{1}{\Delta t \Delta \nu} \iint_{\mathbf{B}_{kr}^{[\Delta t \Delta \nu]}} \mathcal{V}(\mathbf{u}_{pq}(t, \nu)) d\nu dt. \quad (5)$$

In the time-frequency space the bins are sampled equally on each baseline (assuming baseline-independent sampling), while in contrast in uv -space, they are not. Ideally, all spatial frequencies up to the resolution of the longest baseline are sampled in a 2-D continuous sky image. This requires Nyquist sampling of the time-frequency space up to the highest spatial frequencies, corresponding to the longest baselines. This is rarely possible because of the unsampled uv -space “holes” during an observation, the lower spatial frequency cut-off due to physical element limitations and sampling bias in the low spatial frequency region of the uv -space compared to higher spatial frequencies due to baseline distribution. For a fixed time-frequency length, a long baseline will cover a longer track in uv -space compared to a shorter baseline, which results in the lower Fourier modes being oversampled compared to higher Fourier modes. On shorter baselines, the sampling bin width and height are smaller compared to longer baselines; assuming baseline-

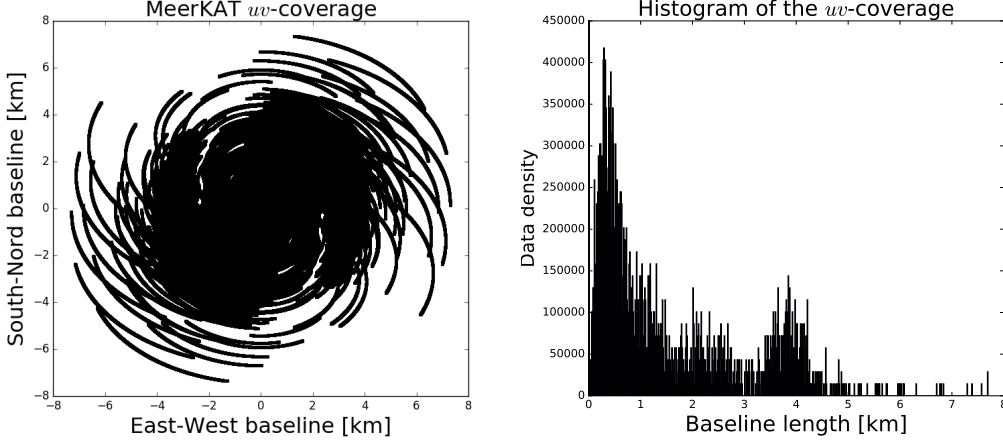


Figure 2. MeerKAT uv -coverage at 1.4 GHz and histogram depicting the data density as a function baselines length, 4 hr observation and 8 MHz bandwidth showing clearly that the data are condensed at the centre. Most of the data at the centre come from the short baselines.

dependent mapping. However, this work considers two major sub-domains. (1) The correlator domain or the $t\nu$ -space where the baselines are sampled equally onto a rectangular grid. (2) The visibility domain or uv -space where the baselines are sampled differently and the overall data are mapped onto elliptical arcs/ribbons.

Let us denote by $\mathbf{B}_{pqkr}^{[uv]}$ the matched uv -space sampling bin, which is baseline-dependent. The relation in Eq. (5) can be rewritten as:

$$\tilde{\mathcal{V}}_{pqkr} = [\mathcal{V}_{pq} \circ \Pi^{[t\nu]}](t_k, \nu_r), \text{ in } t\nu\text{-space or} \quad (6)$$

$$\tilde{\mathcal{V}}_{pqkr} = [\mathcal{V}_{pq} \circ \Pi_{pqkr}^{[uv]}](\mathbf{u}_{pq}(t_k, \nu_r)), \text{ in } uv\text{-space.} \quad (7)$$

Here \circ stands for the convolution operator, and $\Pi^{[t\nu]}$, $\Pi_{pqkr}^{[uv]}$ are normalised boxcar window functions defined in $t\nu$ -space and uv -space respectively. The detailed derivations for these equations are developed in Atemkeng et al. (2016). Eq. (6) and (7) are of importance because they clearly show that visibility averaging is equivalent to convolution at the centre of the sampling bin of the true visibilities and the boxcar window function. We emphasise that the discussion above provides an alternative way to look at decorrelation/smearing. With averaging in effect, a useful mathematical model may be of the following form:

$$\tilde{\mathcal{V}}_{pqkr} = \delta_{pqkr} (\mathcal{V} \circ \Pi_{pqkr}^{[uv]}), \quad (8)$$

where δ_{pqkr} denotes the Dirac delta functions i.e. a single nail sampling function.

2.1 Imaging

To derive the effect of averaging on the image, we can reformulate Eq. (8) as:

$$\tilde{\mathcal{V}}_{pqkr} = \mathcal{F}\{\mathcal{P}_{pqkr}\} \left(\mathcal{F}\{\mathcal{I}\} \circ \Pi_{pqkr}^{[uv]} \right), \quad (9)$$

where the apparent sky \mathcal{I} is the inverse Fourier transform of the ideal visibility measurement $\mathcal{I} = \mathcal{F}^{-1}\{\mathcal{V}\}$ and the point spread function \mathcal{P}_{pqkr} is the inverse Fourier transform of the

sampling function for the baseline pq at the discrete time-frequency bin kr , i.e. $\mathcal{P}_{pqkr} = \mathcal{F}^{-1}\{\delta_{pqkr}\}$. Here \mathcal{F} and \mathcal{F}^{-1} represent the Fourier transform and its inverse respectively. Inverting the Fourier transform of the sum over all baselines of Eq. (9) and sampling at each kr results in an estimate of the sky image i.e. the “dirty image”:

$$\mathcal{I}^D = \mathcal{F}^{-1} \left\{ \sum_{pqkr} W_{pqkr} \tilde{\mathcal{V}}_{pqkr} \right\}, \quad (10)$$

where W_{pqkr} is the weight at the sampled point $pqkr$; in all the extent of the uv -space $\mathcal{W} = \sum_{pqkr} W_{pqkr} \delta_{pqkr}$ in functional form, i.e. the weighted-sampling function. Substituting Eq. (9) into Eq. (10) and applying the convolution theorem, we now have:

$$\mathcal{I}^D = \sum_{pqkr} W_{pqkr} \mathcal{P}_{pqkr} \circ (\mathcal{I} \cdot \mathcal{T}_{pqkr}), \quad (11)$$

with the apparent sky \mathcal{I} now tapered by the baseline-dependent *window response function* \mathcal{T}_{pqkr} , the latter being the inverse Fourier transform of the baseline-dependent boxcar window:

$$\mathcal{T}_{pqkr} = \mathcal{F}^{-1} \left\{ \Pi_{pqkr}^{[uv]} \right\}. \quad (12)$$

Interestingly, Eq. (11) explicitly enforces conditions on the dirty image which has the dependence on all the individual image-plane response (IPR) tapers, \mathcal{T}_{pqkr} . It should be noted that these IPR tapers are not completely arbitrary; in the sense that they depend on each baseline length and orientation. Longer baselines have narrower IPR and are thus prone more to smearing than shorter baselines.

In synthesis imaging, we assume that the sky is a constant signal (transient events are ignored), but a time variable signal is measured because the projected baseline change in orientation and length as the Earth rotates. Also, the frequency coverage and array layout are used to fill in the synthesised aperture, making the signal depending on frequency and array layout. The boxcar window functions are linear but depend on baseline length, which varies with time and frequency: this is why in the entire uv -space, simple averaging is **not** a *true-convolution*

as demonstrated in Atemkeng et al. (2016). We refer this as a “*pseudo-convolution*”. However, if one considers only a single East-West baseline, then simple averaging becomes a *true-convolution* because the lengths of the boxcar window do not change along the uv -track. Simple averaging still remains a *pseudo-convolution* for a baseline with a non-zero South-North component. When considering the entire uv -space then it is not sufficient to simply analyse the boxcar window functions IPRs. As opposed to true-convolution the pseudo-convolution is a linear time-frequency variant system, which leads to complexity in the analysis of the signal conditioning. In practical situations, all the boxcar window functions are window-function-unweighted, moving averages of the measured visibilities, rather than the ideal visibilities. Consider that V_{pqij}^S is the measured visibility sample at $pqij$ with high temporal and spectral resolution. In this sense, we assume that $V_{pqij}^S \equiv V_{pqij}$ if the noise term across all the visibility samples is ignored. Averaging becomes a discrete convolution:

$$\tilde{V}_{pqkr} = \frac{\sum_{i,j \in \mathbf{B}_{kr}} V_{pqij}^S \Pi_{pqkr}^{[uv]}(\mathbf{u}_{pqij} - \mathbf{u}_{pqkr})}{\sum_{i,j \in \mathbf{B}_{kr}} \Pi_{pqkr}^{[uv]}(\mathbf{u}_{pqij} - \mathbf{u}_{pqkr})}, \quad (13)$$

where the set \mathbf{B}_{kr} corresponds to the bin indices of the sampling bin, i.e. $\mathbf{B}_{kr} = \{ij : t_i \nu_j \in \mathbf{B}_{kr}^{[\Delta t \Delta \nu]}\}$.

This work investigates an alternative approach for visibilities sampling, which emphasises that in the entire uv -space all the baselines should be regularly sampled then window function should be applied to shape the FoI. If the window function is a boxcar window or a BDWF then the regular sampling will results to an invariant window length in uv -space, which is now a *true-convolution* in the entire uv -space as opposed to the work discussed in Atemkeng et al. (2016). A true-convolution in the entire uv -space means that in the $t\nu$ -space, the time-frequency sampling intervals now varies across baselines: longer sampling intervals on short baselines and shorter on long baselines. Using this novel approach, the sampling bin defined in Eq. (4) becomes baselines-dependent: the width and height of the sampling bin vary as a function of East-West baselines length. Also, with the novel approach the BDWFs in the $t\nu$ -space are sampled equally but are changing in lengths and resolution across baselines. Each of these properties are shown in Figure 3. Interest in such techniques comes from the fact that:

- There are some longer baselines where the data should be averaged more than some shorter baselines. This can be seen in the histogram of Figure 2, where data are condensed for baseline lengths between ~ 3.5 km and ~ 4.2 km than some shorter baselines. These longer baselines have smaller East-West components and are less prone to decorrelation/smearing, and so the data should be averaged more.
- The sampling bin for a single baseline with a non-zero East-West and South-North components should vary along the baseline uv -track depending on the baseline direction. This variation of the sampling bin should be taken into account for regular sampling in the uv -space.
- The IPR taper for all the baselines may result in the same degree of decorrelation/smearing if the visibilities are regular sampled in the uv -space.
- One may adapt signal processing methods that assume

a *true-convolution* to find the optimal matched IPR. Finding an optimal matched IPR is beyond the scope of this paper, and part of an ongoing study.

3 Baseline-dependent sampling and averaging: BDA

3.1 Effect on the image

An interferometer measures the average visibility over a rectangular time-frequency bin given by Δt and $\Delta \nu$: this is the sampling bin defined in Eq. (4). In $t\nu$ -space, for a fixed length of time-frequency the corresponding sampling bin swept by different baselines in uv -space are not equal: shorter East-West baselines sweep smaller sampling bin and vice-versa. Similarly, for a fixed sampling bin across all baselines in uv -space (baseline-independent sampling bin in uv -space), the corresponding time-frequency intervals in the $t\nu$ -space vary with East-West baseline length: shorter time-frequency intervals on long East-West baselines and longer time-frequency intervals on short East-West baselines. Let us consider a baseline-independent sampling bin in uv -space and let us denote the variant time and frequency intervals by $\Delta \mathbf{u}_{pq} t$ and $\Delta \mathbf{u}_{pq} \nu$ in $t\nu$ -space respectively. The sampling bin becomes baseline-dependent in $t\nu$ -space (indicated here by the extra index \mathbf{u}_{pq} , which is not found in Eq. (4)):

$$\mathbf{B}_{kr}^{[\Delta \mathbf{u}_{pq} t, \Delta \mathbf{u}_{pq} \nu]} = \left[t_k - \frac{\Delta \mathbf{u}_{pq} t}{2}, t_k + \frac{\Delta \mathbf{u}_{pq} t}{2} \right] \times \left[\nu_r - \frac{\Delta \mathbf{u}_{pq} \nu}{2}, \nu_r + \frac{\Delta \mathbf{u}_{pq} \nu}{2} \right]. \quad (14)$$

Figure 3 shows a typical baseline-independent sampling bin in uv -space (top-left) and baseline-dependent sampling bin in $t\nu$ -space (bottom-left). If we denote in function form by \mathcal{D} the area of the baseline-independent sampling bin in uv -space then we have:

$$\mathcal{D} : \mathbf{B}^{[\Delta \mathbf{u}_{pq} t, \Delta \mathbf{u}_{pq} \nu]} \rightarrow \mathcal{R} \\ t, \nu \mapsto d_{\mathbf{u}_{pqkr}},$$

where \mathcal{R} is the set of real numbers. One can decomposed $d_{\mathbf{u}_{pqkr}}$ as the product of the width $d_{\mathbf{u}_{pqk}}$ and height $d_{\mathbf{u}_{pqr}}$ of the sampling bin:

$$d_{\mathbf{u}_{pqkr}} = d_{\mathbf{u}_{pqk}} \times d_{\mathbf{u}_{pqr}}. \quad (15)$$

For $(t_i, \nu_j) \neq (t_k, \nu_r)$, $d_{\mathbf{u}_{pqk}}$ and $d_{\mathbf{u}_{pqr}}$ are given by:

$$d_{\mathbf{u}_{pqk}} = \sum_{t_i \nu_j} \|\mathbf{u}_{pq}(t_i - t_k, \nu)\|, \quad (16)$$

$$d_{\mathbf{u}_{pqr}} = \sum_{t_i \nu_j} \|\mathbf{u}_{pq}(t, \nu_j - \nu_r)\|, \quad (17)$$

where $t_i \nu_j \in \mathbf{B}_{kr}^{[\Delta \mathbf{u}_{pq} t, \Delta \mathbf{u}_{pq} \nu]}$. If the visibilities are regular sampled along all the baselines in the uv -space then for all East-West baselines $\alpha\beta \neq pq$ with $\|\mathbf{u}_{\alpha\beta}\| \neq \|\mathbf{u}_{pq}\|$ the following constraints must be satisfied:

$$d_{\mathbf{u}_{\alpha\beta k}} = d_{\mathbf{u}_{pqk}} \text{ and } d_{\mathbf{u}_{\alpha\beta r}} = d_{\mathbf{u}_{pqr}}. \quad (18)$$

Let us see what Eq. (11) becomes in the case of regular sampling along all the baselines in uv -space. The uv -space boxcar window, $\Pi_{pqkr}^{[uv]}$ is now approximately equal in length

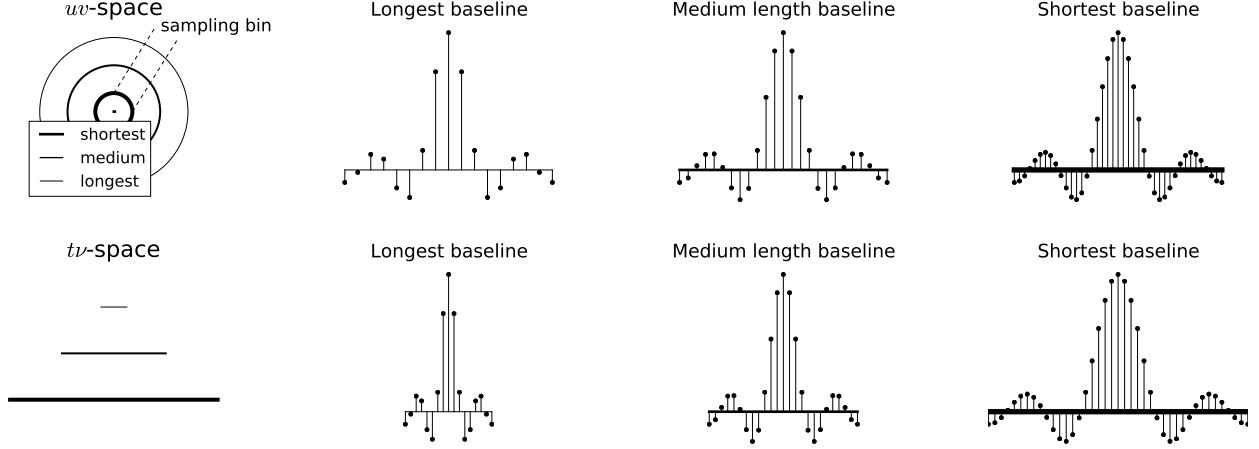


Figure 3. An East-West interferometer array: BDAWF defined in uv -space (top) and in tv -space (bottom). In uv -space, the sampling bin, the window resolution and length remain constant across all the baselines, while the sampling rate varies with respect to the baseline length with shorter baselines oversampled and longer baselines downsampled. In tv -space, all the baselines are sampled equally but the sampling bin, window resolution and length are now varying.

across all East-West baselines, i.e. for all East-West baselines $\alpha\beta \neq pq$:

$$\Pi_{\alpha\beta kr}^{[uv]} \approx \Pi_{pqkr}^{[uv]}. \quad (19)$$

Does this mean that $\mathcal{T}_{\alpha\beta kr} \approx \mathcal{T}_{pqkr}$? The latter will be always true in theory and not in practice. Note that while the length of the boxcar window is equal for all baselines in uv -space, the boxcar window is sampled differently (the top panel of Figure 3 illustrates this in the case where the boxcar window is replaced with a sinc-like window). The boxcar window is downsampled on the longer East-West baselines and oversampled on the shorter East-West baselines, which then results to $\mathcal{T}_{\alpha\beta kr} \neq \mathcal{T}_{pqkr}$. However, if the pre-averaged visibilities are sampled at significantly higher temporal and spectral resolution (at the cost of computation) then one can assume that all these boxcar windows at different baselines are sampled equally. Considering this assumption, we can write:

$$\mathcal{T}_{pqkr} \approx \mathcal{T}_{\alpha\beta kr}. \quad (20)$$

Eq. (11) becomes:

$$\mathcal{I}^D \approx \sum_{pqkr} W_{pqkr} \mathcal{P}_{pqkr} \circ \mathcal{I} \cdot \mathcal{T}, \quad (21)$$

where $\mathcal{T} = \mathcal{T}_{pqkr} \approx \mathcal{T}_{\alpha\beta kr}$ is the smearing response, which is now the effect of a single taper on the image. One can summarise Eq. (21) as:

$$\mathcal{I}^D \approx \mathcal{I}^A \cdot \mathcal{T}, \quad (22)$$

where \mathcal{I}^A is the apparent image corrupted by all the effects that affect the signal from the source to the measurement and noise. The result in Eq. (22) is one of the mathematical derivations achieved in this work, which shows that with BDA or BDAWFs in effect, the dirty image is the apparent sky multiplied by a single taper.

3.2 Implementation with current storage schemes

In practice, most existing software implementations assume that the correlation matrix is a regular grid in time and frequency. Averaging entries in this correlation matrix over long times for short baselines and short times for long baselines results in an irregular grid. A better idea is to map this irregular grid onto a correlation matrix (i.e. regular grid) by either flagging out the supplementary points, or duplicating the averaged values onto these supplementary points.

Flagging: Most of the radio interferometric data reduction software has a flagging capability, through which bad data can be flagged and ignored. For BDA, we exploit this capability to force interferometric data reduction software to ignore some entries of the regularly gridded plane (e.g. the correlation matrix). In the flagging procedure, one has to make sure that the sampling bin contains an odd number of data points in time as well as in frequency. This condition must be verified on all baselines otherwise the average baseline vector may not coincide with the mid-time and mid-frequency vector and this could lead to a phase shift. If this condition is satisfied, the average value is assigned to the midpoint of the sampling bin. The other entries of the sampling bin are flagged. This flag will cause missing samples to be ignored during post-processing.

Duplication: This method consists of duplicating the average value at all entries of the sampling bin in tv -space. While this process is easier to implement than the flagging method, it may not serve the purpose of data compression and/or quick computation for post-processing. It is easier to implement in the sense that one may not care or always verify that the number of visibility points in the sampling bin is an odd number. Furthermore, the data size of the resulting data set remains the same as the pre-averaged data set, since all values are duplicated along the pre-averaged data set. This method may be used in practice for cases where one does not want to estimate the averaged uv -coordinates from the pre-averaged data set.

Semi-duplication and flagging: This method consists of combining the flagging and the duplicate methods in order to benefit from their full advantages. In so doing, we seek both data compression and quick computation, while making implementation easier to handle. The idea is to duplicate the averaged bin along two central entries of the sampling bin if the total number of entries within this sampling bin is even, otherwise, the averaged bin is assigned only to the central point of the sampling bin. Any other entry is then flagged.

3.3 Compression and computation

The compression factor is defined as the ratio between the sizes of the pre-averaged (high-res) data and the averaged (low-res) data. In terms of the number of visibility samples, the high-res data size is:

$$N_{\text{vis}}^{\text{hires}} = N_{\text{bl}} \times N_{\text{sub}} \times N_{\text{pol}} \times N_t^{\text{hires}} \times N_{\nu}^{\text{hires}}, \quad (23)$$

where N_{bl} is the number of baselines, N_{sub} the number of sub-bands, N_{pol} the number of polarisation, N_t^{hires} and N_{ν}^{hires} the number of timeslots and channels of the high-res data respectively. For $n_{pqkr} = n_{pqk} \times n_{pqr}$ number of samples in the sampling bin for a given baseline pq , with n_{pqk} and n_{pqr} the baseline number of time and frequency samples respectively. If one were to adopt a new storage scheme for BDA where there is no flagging or duplicated visibility samples, the data size in terms of number of visibility samples will be:

$$N_{\text{vis}}^{\text{BDA}} = \sum_{pqkr} N_{\text{sub}} \times N_{\text{pol}} \times \frac{N_t^{\text{hires}} \times N_{\nu}^{\text{hires}}}{n_{pqk} \times n_{pqr}}. \quad (24)$$

The compression factor after simplifications is then:

$$\text{CF} = \frac{N_{\text{vis}}^{\text{hires}}}{N_{\text{vis}}^{\text{BDA}}} = N_{\text{bl}} \times \left(\sum_{pqkr} \frac{1}{n_{pqk} \times n_{pqr}} \right)^{-1}. \quad (25)$$

In the case of simple averaging $n_{pqk} = n_t$, $n_{pqr} = n_{\nu}$ with n_t and n_{ν} the number of time and frequency samples averaged on each of the baselines. After simplifying Eq. (25) we have:

$$\text{CF} = n_t \times n_{\nu}. \quad (26)$$

In the following sections, we refer to the compression factor as $\text{CF} = \text{CF}_t \times \text{CF}_{\nu}$, where CF_t and CF_{ν} are the compression factors in time and frequency for the interferometer array respectively. The notations $\text{CF} = \text{CF}_t \times 1$ and $\text{CF} = 1 \times \text{CF}_{\nu}$ imply that the data are compressed only in time by a factor of CF_t and only in frequency by a factor of CF_{ν} respectively. For BDA formalism, the shorter baselines are compressed by much more than CF and the longer baselines by much less, while this corresponds to CF for the interferometer overall compression factor, which remains constant for all the baselines with simple averaging.

The computational cost C^{cost} during the compression of the overall data for an individual interferometer remains equivalent for both BDA and simple averaging if their resulting compressed data are of the same size. The compression cost will scale as:

$$C^{\text{cost}} \sim \mathcal{O}(N_{\text{vis}}^{\text{BDA}} \text{CF}) \quad (27)$$

$$\sim \mathcal{O}(N_{\text{bl}} N_{\nu} \text{CF}) \quad (28)$$

$$\sim \mathcal{O}(N_{\text{bl}} N_{\nu} n_t n_{\nu}), \quad (29)$$

where N_{ν} is the number of visibilities and $\mathcal{O}(N_{\nu} n_t n_{\nu})$ the compression cost on each individual baseline after simple averaging respectively. But note that on each individual baseline the cost C_{pq}^{cost} then varies for BDA which scale as:

$$C_{pq}^{\text{cost}} \sim \mathcal{O}(N_{pqv} n_{pqk} n_{pqr}), \quad (30)$$

with N_{pqv} the baseline-dependent number of resulting visibilities on pq after BDA. For shorter baselines $C_{pq}^{\text{cost}} \ll \mathcal{O}(N_{\nu} n_t n_{\nu})$ while on the longer baselines $C_{pq}^{\text{cost}} \gg \mathcal{O}(N_{\nu} n_t n_{\nu})$ but the overall computation cost leads to:

$$C^{\text{cost}} \sim \mathcal{O}\left(\sum_{pqkr} N_{pqv} n_{pqk} n_{pqr}\right) \quad (31)$$

$$\sim \mathcal{O}(N_{\text{bl}} N_{\nu} n_t n_{\nu}). \quad (32)$$

3.4 Noise and noise penalty

Let us look at what the estimates theoretical thermal noise induced by BDA become in each of the averaged visibilities. If for the high-res data, we assume that the noise term has constant r.m.s σ_s across all the baselines, then the noise induced in each of the BDA visibility is given by:

$$\sigma_{pqkr, \text{BDA}}^2 = \frac{1}{n_{pqkr}^2} \sum_{i=1}^{n_{pqkr}} \sigma_s^2 = \frac{\sigma_s^2}{n_{pqkr}}. \quad (33)$$

Let us assume that the noise is uncorrelated across averaged visibilities. The average of the squared error norm in each pixel of the dirty image is then:

$$\sigma_{pix, \text{BDA}}^2 = \frac{(\sum_{pqkr} W_{pqkr}^2 \sigma_{pqkr, \text{BDA}}^2)}{(\sum_{pqkr} W_{pqkr})^2}, \quad (34)$$

which for natural image weighting $W \equiv 1$ simplifies to:

$$\sigma_{pix, \text{BDA}}^2 = \left(\frac{\text{CF} \sigma_s}{N_{\text{vis}}^{\text{hires}}} \right)^2 \sum_{pqkr} \frac{1}{n_{pqkr}}. \quad (35)$$

It is clear that the noise induced by BDA is completely different across baseline visibility samples because the number of averaged samples are quite different; this is expected from Eq. (33). In the case of simple averaging, Eq. (35) is reduced to:

$$\sigma_{pix, \text{AVG}}^2 = \frac{\text{CF}}{N_{\text{vis}}^{\text{hires}} n_t n_{\nu}} \sigma_s^2 \quad (36)$$

$$= \frac{1}{N_{\text{vis}}^{\text{hires}}} \sigma_s^2 = \frac{1}{N_{\text{vis}}^{\text{AVG}} n_t n_{\nu}} \sigma_s^2, \quad (37)$$

where $N_{\text{vis}}^{\text{AVG}}$ is the number of visibilities in the simple averaged data, the index AVG stands for simple averaging. Refer to Appendix A for a detailed proof of Eq. (35) and (37). The derivation in Eq. (37) matches the result of the mathematical expectation of the squared error norm in each pixel of the dirty image in the case of simple averaged as shown in Atemkeng et al. (2016). It is clearly shown in Eq. (37) that $\sigma_{pix, \text{BDA}} = \sigma_{pix, \text{AVG}}$. Note that this is always true because both compression methods use a boxcar window as a weighting function in the uv -space which means that all the pre-averaged visibilities are equally weighted for both BDA and simple averaging. If we compress the visibilities using a BDWF $X(u, v)$ or a BDAWF $X_{\text{BDA}}(u, v)$, the noise term still remains different per each visibility $pqkr$:

$$\sigma_{X_{pqkr}}^2 = \frac{\sum X^2(\mathbf{u}_{pqij} - \mathbf{u}_{pqkr})}{[\sum X(\mathbf{u}_{pqij} - \mathbf{u}_{pqkr})]^2} \sigma_s^2, \quad (38)$$

where the sums are taken over the baseline-independent sampling bin indices and

$$\sigma_{X_{pqkr}, \text{BDA}}^2 = \frac{\sum X_{\text{BDA}}^2(\mathbf{u}_{pqij} - \mathbf{u}_{pqkr})}{\left[\sum X_{\text{BDA}}(\mathbf{u}_{pqij} - \mathbf{u}_{pqkr})\right]^2} \sigma_s^2, \quad (39)$$

where the sums are taken over the baseline-dependent sampling bins indices.

Eq. (38) and (39) are of critical importance on the squared error norm in each pixel of the dirty image and so they merit detailed explanation:

- 1) In uv -space, the length of the window $X(u, v)$ (BDWF) remains constant across all baselines while the window resolution varies on different baselines: in this sense, $X(u, v)$ is baseline-dependent. Because the length of $X(u, v)$ is constant along all the baselines, the compression factor also remains constant across all the baselines, as when applying a simple averaging (see Atemkeng et al. (2016)).
- 2) In uv -space, the window $X_{\text{BDA}}(u, v)$ (BDAWF) varies in length (hence the extrat index $_{\text{BDA}}$) and resolution across all baselines. Because the length of $X_{\text{BDA}}(u, v)$ varies along baselines, the compression factor thus varies on different baselines (looking back to Figure 3).
- 3) If one were to constrain the compression factor CF to be equal for both ‘‘BDWF’’ and ‘‘BDAWF’’, the squared error norm in each pixel of the dirty image will change radically. This can be understood by looking at steps 1) and 2): $X(u, v)$ and $X_{\text{BDA}}(u, v)$ produce completely different weights for each (u, v) point. In other words, $X(u, v) \neq X_{\text{BDA}}(u, v)$ for a given (u, v) point.

The visibility noise penalty induced by BDA or BDAWF is the relative increase in noise over simple averaging:

$$\Xi_{X_\mu} = \frac{\sigma_{X_\mu}}{\sigma_{\text{AVG}}}. \quad (40)$$

Here, $\sigma_{\text{AVG}} = \sigma_s^2/(n_i n_\nu)$ is the noise on the simple averaged visibility and σ_{X_μ} is either the noise induced by BDA or BDAWF. The centre pixel noise penalty in the image with imaging weights W :

$$\Xi_\mu^W = \frac{\sigma_{pix, X}^2}{\sigma_{pix}^2} = \frac{(\sum_\mu W_\mu^2 \Xi_{X_\mu}^2)}{(\sum_\mu W_\mu)^2}. \quad (41)$$

Note that the noise penalty properties induced by overlapping BDWFs defined in Atemkeng et al. (2016) remains valid for BDA and BDAWF.

Simulations confirm the theoretical noise penalty estimate discussed above. The simulation consists of two datasets; the high-res and the low-res datasets using the MeerKAT telescope. The high-res dataset is simulated with $\sigma_s = 1$ Jy thermal noise during a total period of 4 hr with 1 s integration time and 84 MHz bandwidth divided into channels of 84 kHz. We then compress the high-res using simple averaging, then BDA and BDAWFs, and save the resulting visibilities to the low-res dataset. For both compression schemes, we fixed the compression factors to CF=15×10 and CF=30×20, which then correspond to simple averaging across 15 s × 0.84 MHz and 30 s × 1.68 MHz respectively. We use the sinc tuned to a FoI of 1.3° with overlap factors of 6 × 5 of the baseline-dependent sampling bins. For each case of compression, we then consider the r.m.s pixel noise as an estimator of σ_{pix} (simple averaging) and $\sigma_{pix, X}$ (BDA

Filters	Ξ theo	Ξ sim
BDA 15 s × 0.84 MHz	1.00	1.03
BDA 30 s × 1.68 MHz	1.00	1.004
BDA-sinc-6×5-1.3deg 15 s × 0.84 MHz	1.19	1.23
BDA-sinc-6×5-1.3deg 30 s × 1.68 MHz	1.51	1.56

Table 1. A comparison of image noise penalties associated with different BDA and BDAWFs, computed analytically (Ξ theo) vs. simulations (Ξ sim). The analytical noise penalty for BDA is equal to 1, this is straightforward by looking at Eq. (35) and (37).

or BDAWFs). The analytical estimated and simulated noise penalty are compared in Table 1. Results confirm that both analytical estimates and simulations agree.

4 Simulations and results

Having explored the mathematics and implementation of BDA, we now turn to the simulation aspects. The simulations are performed with the MeerKAT and the EVN telescopes. The simulated images are not calibrated and deconvolved to avoid introducing additional effects relative to calibration and/or deconvolution algorithms. Two test scenarios are considered and both of them are simulated using MeqTrees (Noordam & Smirnov 2010):

- We consider a 1 Jy point source at various sky positions, with no noise or other corruptions included. We evaluate the efficiency of a BDA correlator using two different procedures. Firstly, we simulate the source at a fixed sky position, apply BDA, BDAWFs and measure the compression effects separately on each baseline. Secondly, we simulate the point source at various angular distances from the phase centre and apply BDA and BDAWFs, thereby evaluating the interferometer cumulative decorrelation effects on all baselines. We measure the source peak amplitude in each dirty image after compression. Since each dirty image corresponds to a single source, the peak gives us the degree of smearing associated with a given compression method and compression factor.

- The PB on its own could be used for source suppression, the higher the frequency the less sources out of the FoI contaminate the image. Tests are performed when the PB is included during the simulations, BDA and BDWFs are applied to evaluate the combined degree of suppression for sources out of the FoI.

4.1 Application to MeerKAT data

4.1.1 Source amplitude and East-West baselines

The experiment in Figure 1 is repeated. The simulation consists of two high-res measurement sets (MSs), each with a source at 2.25 deg relative to the observation phase centre. Two low-res MSs are generated to receive the compressed visibilities. The results of the decorrelation when applying simple averaging and BDA are compared in the top panel of Figure 4 and the BDA compression factors achieved with the simulation are plotted in the bottom panel of Figure 4.

- Time decorrelation and compression factors, Figure 4 (left): the MS consists of 64 frequency channels of 84 kHz width each, and 7200 s timeslots of 1 s integration time.

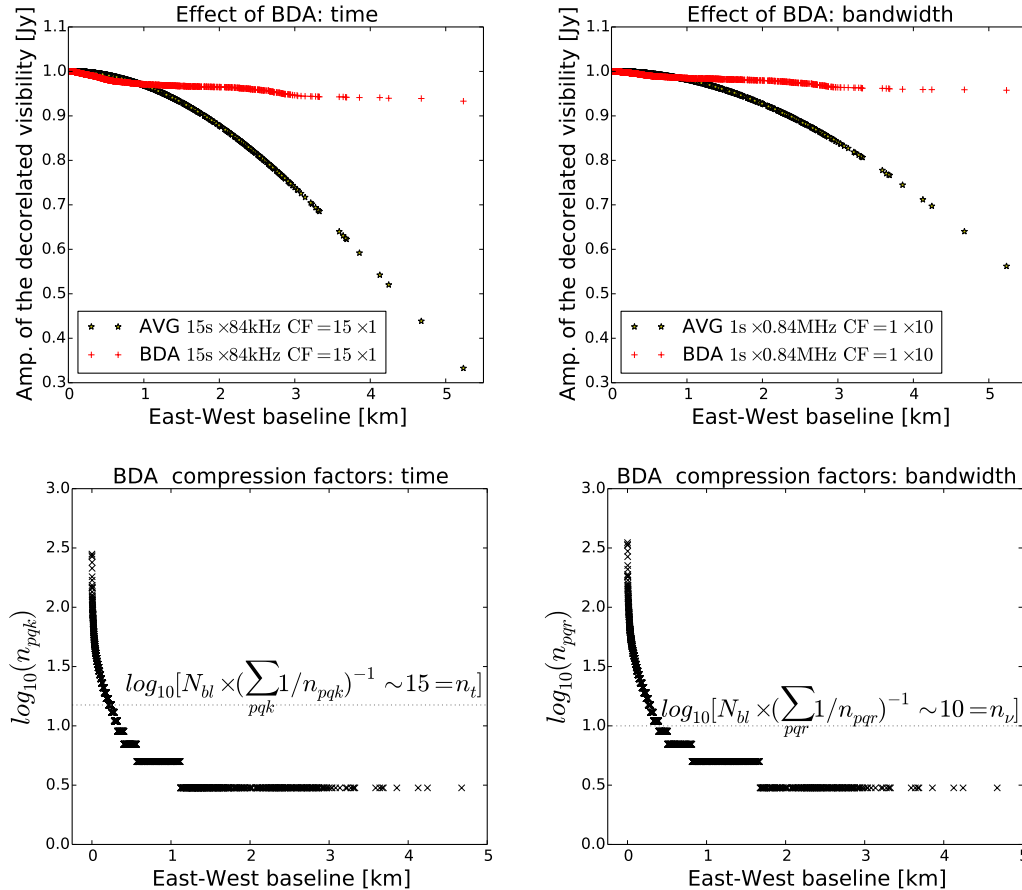


Figure 4. (Top) Amplitude loss: the apparent intensity of a 1 Jy source at 2.25 deg as seen by MeerKAT at 1.4 GHz, as a function of East-West baseline components; (left) compression carried out only in time with compression factor fixed to 15 time-bins; (right) compression is carried out only in frequency with compression factor fixed to 10 frequency-bins. (Bottom) Baseline-dependent compression factors in time (left) and frequency (right) both in logarithm scale as a function of East-West baseline length.

The compression factor is fixed to $CF=15 \times 1$ for both simple averaging and BDA. For BDA, the shorter baselines are compressed by a lot more than 15 and the longer baselines by a lot less, while for simple averaging this corresponds to 15 factor of compression along all the baselines.

- Bandwidth decorrelation and compression factors, Figure 4 (right): The MS consists of 100 timeslots of 1 s integration, and 1000 frequency channels of 84 kHz (total bandwidth of 84 MHz). The compression factor is fixed to $CF=1 \times 10$ both for simple averaging and BDA. For BDA, the shorter baselines are compressed by a lot more than 10 and the longer baselines by a lot less, and for simple averaging this corresponds to a compression factor of 10.

It is clearly noticeable in the top panels of Figure 4 that on shorter baselines, the smearing rates of simple averaging and BDA are approximately equivalent despite the little percentage of signal lost with BDA in the region between 0.2 km and 0.8 km. This can be understood by looking at the MeerKAT histogram depicted in Figure 2, this is the region where one wants to compress the data as bigger as possible. However, for a source at 2.25 deg and at these BDA compression factors the degree of the decorrelation remains approximately equal across all the baselines. This result confirms

our mathematical prediction in Eq. (20). It appears from the simulated time and frequency BDA compression factors depicted in the bottom of Figure 4 that the data are compressed more in frequency than in time. This is because, for MeerKAT, the uv -track along 0.84 MHz is smaller than the uv -track along 15 s. We can still constrain the compression factors to be equal in both time and frequency, in principle, the shape of the 2-D uv -track should be square-like. To derive this, we note that the averaged bandwidth must be equal to $w_e \nu_r \Delta t$, where the constant w_e , is the Earth rotation velocity (Thompson et al. 2001).

4.1.2 Source amplitude and distance from the phase centre

We simulate data at high time-frequency resolution of 1 s integration during 4 hr and 84 kHz channels width for a total bandwidth of 84 MHz centred at 1.4 GHz. The sky model is a single 1 Jy point source at a given distance from the phase centre. Three MSs are generated to store the compressed visibilities:

- Two MSs contain the compressed visibilities for 15 s \times 0.84 MHz and 30 s \times 1.68 MHz, this result in compression factors of $CF=15 \times 10$ and $CF=30 \times 20$ respectively.

- A third MS to receives the compressed visibilities for BDA and BDAWFs. This MS is a copy of the high-res MS where the flagging implementation for BDA described in Sect. 3.2 is applied. Two compression factors are adopted for the BDA and BDAWFs: $CF=15\times 10$ and $CF=30\times 20$.

Figure 5 shows the performance of different compression schemes and compression factors associated with their noise penalty. BDA applied to a sinc-like BDWF is considered in this test and is turned to three different FoI settings, as indicated by the plot: 0.65 deg, 1.32 deg and 2.25 deg. The results can be alternatively appreciated by regarding the performance of BDAWFs:

BDA with $CF=15\times 10$ provides good results in flux recovery, i.e. for 6% smearing we can image up to 4.5 deg FoI, while simple averaging at the same compression factor can only recover this FoI at 10% smearing. The BDA with compression factor $CF=30\times 20$ still provides better source recovery compared to simple averaging at the same compression factor. We can also note that at the same compression factor, the source suppression performance of BDA is worse than that of simple averaging.

At the different compression factors, we see that all the BDAWFs filters provide excellent performance in source recovery and far-field suppression compared to simple averaging or BDA: smearing across the FoI is less than 2% (horizontal grey dashed-line), and out-of-FoI suppression is almost two orders of magnitude higher than simple averaging or BDA. Note the tapering behaviour for BDAWFs at the different compression factors. As the compression factor increases, the response of BDAWFs becomes **flat**: this clearly illustrates their excellent performance. The reason for this is that, a unique sinc-like window function is applied on all the baselines (recall from Figure 3). For larger compression factors the sinc-like window function becomes more proximate to the “sinc”, which results in a more optimal “boxcar-like” taper in the image domain. In general, the noise penalty does depend on the compression scheme and parameters, this is the case for BDAWF, where all the parameters i.e. compression factors, overlapping bins and FoI result in noise penalty-dependent.

4.1.3 Relative SNRs using MeerKAT data

Simulations are used to separate the variables S_{smear} , C_{noise} and T_{noise} in Eq. (2). The simulated MS in Sect. 4.1.2 is reused. We consider to evaluate the SNR of an image of ~ 0.5 square degree centered at 0.65 deg, 1.32 deg and 2.25 deg. For each case, we know S_{smear} from Figure 5. To evaluate the contamination, and for each case, we simulate two sources: a nearby source of 1 Jy (1 deg away from each case) and a distant source of 10 Jy (20 degrees away from from each case), and make an image. The image will be empty, except for the contribution from these two sources. For the thermal noise, an empty sky is simulated with 1 Jy thermal noise for each of the cases listed above. The different compression methods are applied and their resulting SNRs are listed in Table 2. Results show that our compression technique demonstrates better performance in SNR when compared to simple averaging. Comparatively, using BDAWFs provide the best performance in SNR, up to a factor of ~ 4 higher than simple averaging or BDA. Note that in regions

where the source suppression response of BDAWFs kicks in, the SNR quickly drops, since BDAWFs are suppressing the source signal itself at this point.

4.1.4 BDAWFs combined with the primary beam and source suppression

The additional degree of source suppression provided by BDAWFs augments the source suppression provided by the PB, as investigated by e.g. (Mort et al. 2016). Note that BDA by itself (without window functions) actually provides “less” source suppression than simple averaging, at the same compression factor.

In this section, we investigate and compare the combined suppression factor achieved by the PB and averaging, BDA and BDAWFs. A PB model for MeerKAT at 1.4 GHz along with a nearby 20 Jy source located at the second sidelobe of the PB is simulated using the MS described in Sect. 4.1.2. We supposed imaging up to the FWHM of the MeerKAT PB at 1.4 GHz (i.e. 0.65 deg away from the field centre). Three filters are considered and compared, AVG $15\text{ s} \times 0.84\text{ MHz}$, BDA $15\text{ s} \times 0.84\text{ MHz}$ and BDA-sinc- $6\times 5-1.3\text{deg}$ $15\text{ s} \times 0.84\text{ MHz}$ both having for compression factor $CF=15\times 10$. Figure 6 shows dirty images of size 40×40 arcmin at different pixel scales. These images should be empty except the contamination from the nearby source. The top-left and top-right images of Figure 6 show the high-res (i.e. image produced with the pre-averaged MS) and the simple averaged images respectively. The bottom-left and bottom-right images are produced after applying BDA $15\text{ s} \times 0.84\text{ MHz}$ and BDA-sinc- $6\times 5-1.3\text{deg}$ $15\text{ s} \times 0.84\text{ MHz}$ respectively. For both cases, the high-res image is confusion noises dominated across the FoI. The compressed images show a more confusion noise-free images. Unlike BDA that considers only a flux recovery in the image domain, BDAWFs consider both flux recovery in the given FoI and source suppression out of this FoI. This is clearly seeing in Figure 6 that BDA on its own does not remove the contamination than simple averaging but BDAWF does remarkably well.

4.2 BDAWFs and the EVN

In VLBI the baselines are so long (up to ~ 10000 km) that the FoV is always limited, and normally it is only a tiny fraction of the PB at the FWHM because of decorrelation due to time and bandwidth averaging. To keep decorrelation/smearing at acceptable level one may apply wide-FoV correlation, but handling the resulting data volumes has been challenging (e.g. Chi et al. (2013)). Another solution is to *wv*-shift wide-field correlated data to various phase centres and apply averaging then to obtain a number of smaller FoV within the PB (Morgan et al. 2011; Ruiz et al. 2017). This has been fully implemented in the EVN Software Correlator (SFXC; Keimpema et al. (2015)). Multi-phase centre correlation makes milliarcsecond-resolution imaging of a-priori known sources spread over a wide-FoV possible, this has now been applied routinely at the EVN. But some applications (e.g. transient search within the full PB in VLBI data, or to build up a wide-FoV EVN archive) would require storing the raw data from all telescopes, however, this results in very large volumes unless there are alternative approaches. We investigate the possibility of using BDA and

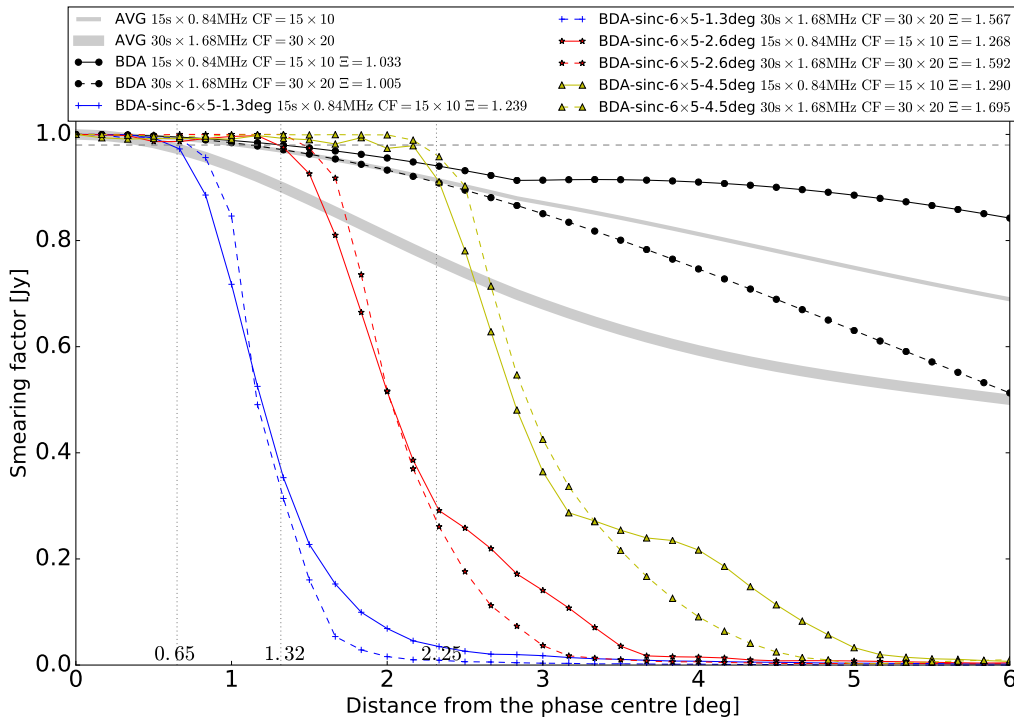


Figure 5. Amplitude loss: the apparent intensity of a 1 Jy source as seen by the MeerKAT telescope at 1.4 GHz as a function of distance from phase centre, for simple averaging with $15 \text{ s} \times 0.84 \text{ MHz}$ and $30 \text{ s} \times 1.68 \text{ MHz}$ bins, and for BDA and BDWFs. The compression factor is fixed to $\text{CF}=15 \times 10$ and $\text{CF}=30 \times 20$ for all the compression methods.

FILTERS	0.65 deg	1.32 deg	2.25 deg
AVG $15 \text{ s} \times 0.84 \text{ MHz}$	16.827	16.437	15.672
BDA $15 \text{ s} \times 0.84 \text{ MHz}$	14.767	14.544	14.072
BDA-sinc-6x5-1.3deg $15 \text{ s} \times 0.84 \text{ MHz}$	64.354	11.590	1.144
BDA-sinc-6x5-2.6deg $15 \text{ s} \times 0.84 \text{ MHz}$	40.256	64.538	9.554
BDA-sinc-6x5-4.5deg $15 \text{ s} \times 0.84 \text{ MHz}$	32.576	32.569	60.249

Table 2. Simulated SNR as described in Eq. (2), i.e. $\text{SNR} \approx S_{\text{smear}} / (C_{\text{noise}} + T_{\text{noise}})$, where S_{smear} , C_{noise} and T_{noise} are defined as the signal of a source of interest, and the contamination signals that affect the signal of interest and the thermal noise respectively. Here $T_{\text{noise}} = \sigma_{\text{pix},X}$ defined in Sect. 3.4.

BDWFs in VLBI to preserve a significant fraction of the PB while significantly reducing the data volume. We repeated the simulation scenarios described in Sect. 4.1.2 using the full EVN (i.e. Badary, Effelsberg, Hartebeesthoek, Jodrell Bank, Medicina, Noto, Onsala, Shanghai, Svetloe, Torun, Westerbork, Zelenchukskaya) at 1.6 GHz. The results are given in Figure 7. It can be seen that for a certain compression rate with simple averaging that would result in a FoI of 6 arcmin, an equivalent compression rate using BDA or BDWFs would result in a FoI of 18 arcmin. We also note that, if one aims at imaging a FoI of 18 arcmin with simple averaging, then this is possible with BDA reducing data by a factor of 9.38, and the factor can be even higher with BDWFs. While these initial tests are very promising, in VLBI there is a significant trade-off in sensitivity and resolution, therefore the best approach should be investigated in detail independently for each science application.

5 Conclusion and perspectives

As discussed above compression of visibilities by simple averaging shows that decorrelation/smearing is more significant on longer baselines than shorter ones and that decorrelation can only be avoided if the correlator performs the averaging procedure over smaller bins, which however results in high data rates. We now make predictions pertaining to sample the visibilities regularly across all the baselines in the entire uv -space and apply BDA and BDWFs. Intuitively, in the time-frequency space (or the correlator domain) this corresponds to averaging within sufficiently large sampling bin for shorter baselines, while the longer baselines are averaged within shorter sampling bin. The question is then whether such averaging technique will not only decrease smearing within the observation FoI, but, also reduce the data size. The second question pertains to calibration issues for this method given that calibration is a complex visibilities correction process. BDA could introduce complexity further down the line: it could, for example, mean that a dynamic calibration solution interval would become necessary. This implies

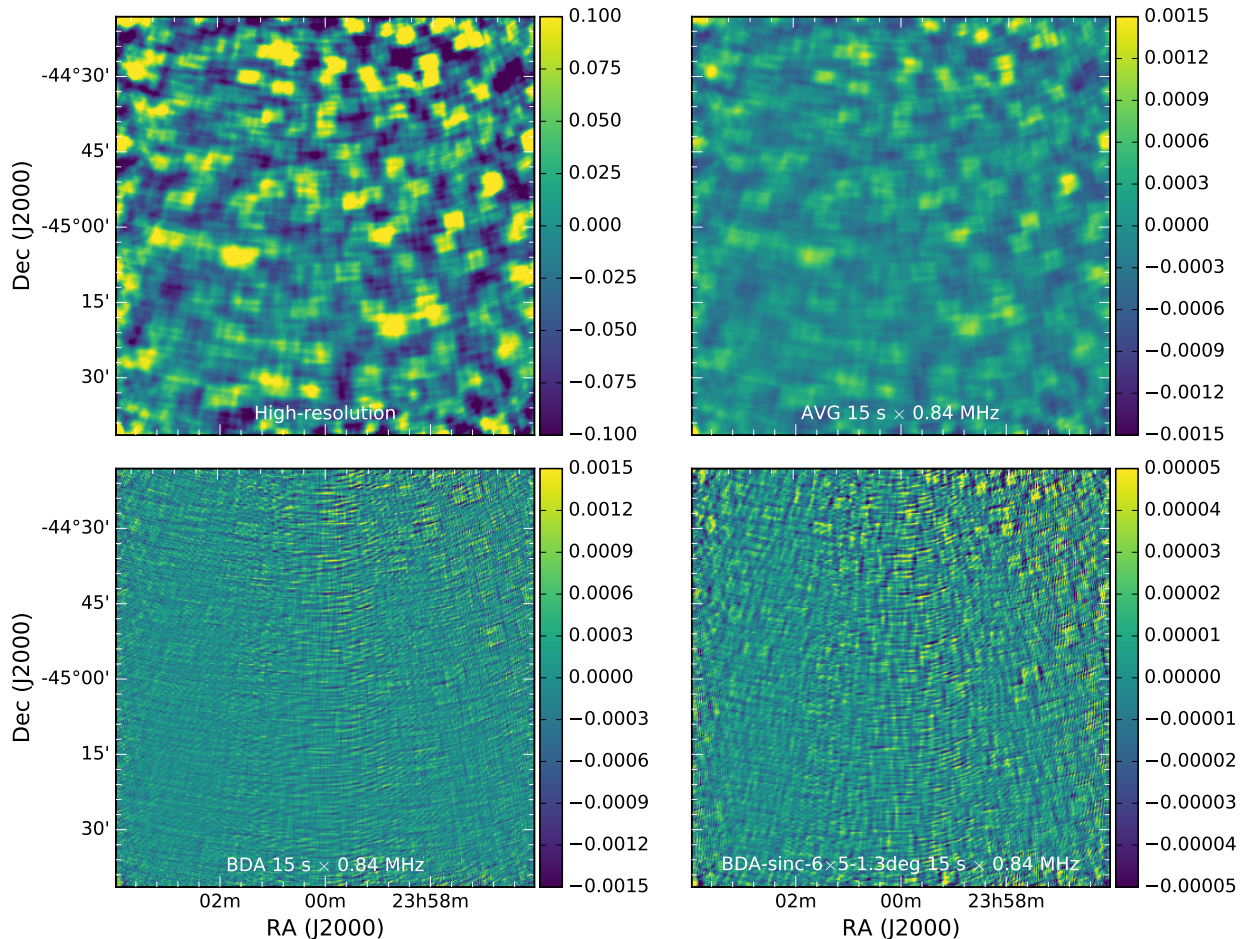


Figure 6. Contamination in the FoI from a 20 Jy source located at the second null of the MeerKAT primary beam. Initially, the data is imaged without data compression been carried out (top-left panel). After data compression is applied using AVG $15 \text{ s} \times 0.84 \text{ MHz}$ (top-right), BDA $15 \text{ s} \times 0.84 \text{ MHz}$ (bottom-left) and BDA-sinc- $6 \times 5 - 1.3 \text{ deg } 15 \text{ s} \times 0.84 \text{ MHz}$ (bottom-right). The colourbars of the images are in Jansky and are in different scales. BDAWFs offer better reduction in source contamination compared to AVG $15 \text{ s} \times 0.84 \text{ MHz}$ and BDA $15 \text{ s} \times 0.84 \text{ MHz}$.

that the calibration solution interval will change differently with baselines and each of the frequency and/or time intervals.

We have established that BDA by itself can only achieve data compression but not FoI shaping: BDA does decrease smearing over the FoI, while on the other hand, sources out-of-FoI are not suppressed compared to simple averaging. We have found that BDAWFs result in excellent tapering behaviour, which can decrease smearing to about 2% or less over a selected FoI, with out-of-FoI source suppression almost two orders of magnitude higher than simple averaging, while the data are compressed at the same rate.

We should note that like simple averaging, BDA and BDAWFs also distort the point spread function (PSF), which becomes position dependent and reacts differently compared to simple averaging. However, for an efficient use of BDA and BDAWFs, one requires to predict this PSF at different sky positions during deconvolution. There exists a faceting imaging framework that accounts for this PSF variation during deconvolution when applying BDA (see

DDFacet (Tasse et al. 2017)). DDFacet uses the brute-force approach to compute the PSF at the centre of each facet, and this PSF is used to deconvolve the facet. However, a brute-force computing load is tolerable for small size facets. For large facets and for any non-faceting deconvolution algorithm an approximation based method to derive all these PSFs must be implemented with the aims to reduce computing cost (Atemkeng et al. 2018, in prep.).

This paper opens up several possibilities for future work. Firstly, designing an optimally matched filter for a BDAWF is an interesting avenue of further research. In practical situations, the IPR of a sinc-like lowpass filter is far from ideal in the sense that a sinc-like filter is band-limited (zero outside some intervals) and sampled. Filter design theory for lowpass filters could, therefore, be used to explore an ideal IPR, by using an approximation to define the ideal filter coefficients and parameters, such as the passband, the transition band and the stopband. The second avenue involves evaluating the degree of source suppression as a function of array layout and BDAWFs parameters, i.e. the pass-

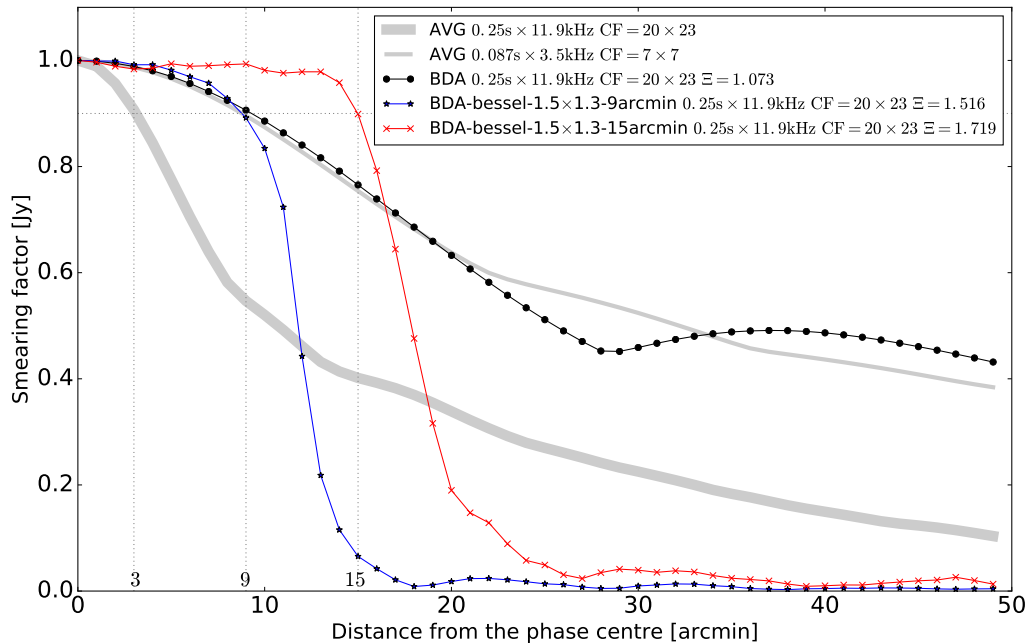


Figure 7. Amplitude loss: the apparent intensity of a 1 Jy source as seen by EVN at 1.6 GHz as a function of distance from phase centre. Results show that the data can be compressed a lot more than a factor of 9.38 using BDAWFs.

band, transition band, stopband and the size of the filter. The third avenue of exploration consists of investigating and exploring calibration with BDA and BDAWFs. Currently, BDA and BDAWFs can only be used post-calibration. Exploring the calibration parameters for BDA and BDAWFs could open a new research avenue in radio interferometry, in view of the effective use of BDA and BDAWFs. Another possible work on BDA will be to explore a possible new storage scheme to take full advantage of the compression capabilities of BDA. In this work, we have considered and used only data structures that a MS and other software packages we used can support. The MS has a lot of flagging entries that still reside in memory.

Finally, this document was restricted to simulations. The next step will be to implement each of the techniques presented in this work in practical research scenarios, e.g. applying the filters to real interferometric data.

ACKNOWLEDGEMENTS

This work is based upon research supported by the South African Research Chairs Initiative of the Department of Science and Technology and National Research Foundation. The European VLBI Network is a joint facility of independent European, African, Asian, and North American radio astronomy institutes. M. Atemkeng is grateful to Tammo Jan Djimeka for valuable discussions on BDA and its applicability to LOFAR real data during his visit at ASTRON. The visit to ASTRON was made possible by the FP7 MID-PREP program. We thank our colleagues Kshitij Thorat, Modhurita Mitra, Etienne Bonnassieux, Diana G. Klutse

and Sphehile Makhathini for their insights and comments on early drafts of this paper. We would also like to thank Khan Asad for making available the MeerKAT primary beam model used in Sect. 4.1.4. The authors would like to thank the reviewer for his valuable comments and suggestions that strongly improved the quality of the paper.

REFERENCES

- Atemkeng M., Smirnov O., Tasse C., Foster G., Jonas J., 2016, *Monthly Notices of the Royal Astronomical Society*, 462, 2542
- Atemkeng M., Smirnov O., Tasse C., Foster G., Makhathini M., 2018, in prep.
- Chi S., Barthel P., Garrett M., 2013, *Astronomy & Astrophysics*, 550, A68
- Cotton W., 1999, in *Synthesis Imaging in Radio Astronomy II Vol. 180, Special problems in imaging*. p. 357
- Cotton W. D., 1989, in *Synthesis Imaging in Radio Astronomy Vol. 6, Special problems in imaging*. p. 233
- Dewdney P. E., Hall P. J., Schilizzi R. T., Lazio T. J. L., 2009, *Proceedings of the IEEE*, 97, 1482
- Gaylard M., Bietenholz M., Combrinck L., Booth R., Buchner S., Fanaroff B., MacLeod G., Nicolson G., Quick J., Stronkhorst P., et al., 2014, arXiv preprint arXiv:1405.7214
- Hamaker J., Bregman J., Sault R., 1996, *Astronomy and Astrophysics Supplement Series*, 117, 137
- Johnston S., Taylor R., Bailes M., Bartel N., Baugh C., Bietenholz M., Blake C., Braun R., Brown J., Chatterjee S., et al., 2008, *Experimental astronomy*, 22, 151

- Jonas J. L., 2009, Proceedings of the IEEE, 97, 1522
- Keimpema A., Kettenis M., Pogrebenko S., Campbell R., Cimó G., Duev D., Eldering B., Kruithof N., van Langevelde H., Marchal D., et al., 2015, Experimental Astronomy, pp 1–21
- Lonsdale C. J., Doleman S. S., Oberoi D., 2004, Experimental Astronomy, 17, 345
- Mitra M., Makhathini S., Foster G., Smirnov O., Perley R., 2015, 2015 International Conference on Electromagnetics in Advanced Applications (ICEAA), pp 494–497
- Morgan J. S., Mantovani F., Deller A., Bricken W., Alef W., Middelberg E., Nanni M., Tingay S., 2011, Astronomy & Astrophysics, 526, A140
- Mort B., Dulwich F., Razavi-Ghods N., de Lera Acedo E., Grainge K., 2016, Monthly Notices of the Royal Astronomical Society, p. stw2814
- Noordam J. E., Smirnov O. M., 2010, Astronomy & Astrophysics, 524, A61
- Parsons A. R., Backer D. C., 2009, The Astronomical Journal, 138, 219
- Parsons A. R., Liu A., Ali Z. S., Cheng C., 2016, The Astrophysical Journal, 820, 51
- Ruiz N. H., Middelberg E., Deller A., Norris R., Best P., Bricken W., Schinnerer E., Smolcic V., Delvecchio I., Momjian E., et al., 2017, arXiv preprint arXiv:1707.07512
- Sabater J., Sánchez-Expósito S., Best P., Garrido J., Verdes-Montenegro L., Lezzi D., 2017, Astronomy and Computing, 19, 75
- Smirnov O., 2011a, Astronomy & Astrophysics, 527, A107
- Smirnov O. M., 2011b, Astronomy & Astrophysics, 527, A106
- Tasse C., Hugo B., Mirmont M., Smirnov O., Atemkeng M., Bester L., Bonnassieux E., Hardcastle M., Lakhoo R., Girard J., et al., 2017, arXiv preprint arXiv:1712.02078
- Thompson A. R., Moran J. M., Swenson G. W., 2001
- Van Haarlem M., Wise M., Gunst A., Heald G., McKean J., Hessels J., De Bruyn A., Nijboer R., Swinbank J., Fallows R., et al., 2013, Astronomy & Astrophysics, 556, A2
- Zarka P., Tagger M., Denis L., Girard J., Konovalenko A., Atemkeng M., Arnaud M., Azarian S., Barsuglia M., Bonafede A., et al., 2015, in Antenna Theory and Techniques (ICATT), 2015 International Conference on Nenufar: Instrument description and science case. pp 1–6

APPENDIX A: MATHEMATICAL DETAILS FOR THE NOISE VARIANCE

Assuming an uncorrelated noise across the BDA averaged visibilities, the variance in each pixel in the uncleaned map for any weighting scheme W is derived as:

$$\sigma_{pix,BDA}^2 = \frac{\sum_{pqkr} W_{pqkr}^2 \sigma_{pqkr,BDA}^2}{(\sum_{pqkr} W_{pqkr})^2}, \quad (1)$$

Setting $W \equiv 1$ (natural weighting), we have:

$$\sigma_{pix,BDA}^2 = \frac{\sum_{pqkr} \sigma_{pqkr,BDA}^2}{(N_{vis}^{lores})^2}, \quad (2)$$

where N_{vis}^{lores} is the total number of visibilities interfering the uv -space after BDA. Recall that $\sigma_{pqkr,BDA}^2 = \sigma_s^2/n_{pqkr}$ see

Eq. (33). Eq. (2) leads to:

$$\sigma_{pix,BDA}^2 = \left(\frac{\sigma_s}{N_{vis}^{lores}} \right)^2 \sum_{pqkr} \frac{1}{n_{pqkr}}. \quad (3)$$

We defined in Eq. (25) the compression factor as $CF = N_{vis}^{hires}/N_{vis}^{lores}$, thus $N_{vis}^{lores} = N_{vis}^{hires}/CF$ replacing the latter in Eq. (3), we then have:

$$\sigma_{pix,BDA}^2 = \left(\frac{CF\sigma_s}{N_{vis}^{hires}} \right)^2 \sum_{pqkr} \frac{1}{n_{pqkr}}, \quad (4)$$

which is the result in Eq. (35). In the case of simple averaging, where the time-frequency compression factor remains constant across all the interferometer baselines (i.e. $n_{pqkr} = n_t n_\nu = CF$), the sum in Eq. (4) will now yield to:

$$\sum_{pqkr} \frac{1}{n_{pqkr}} = \frac{1}{n_t n_\nu} N_{vis}^{lores}. \quad (5)$$

If one replace Eq. (5) in Eq. (4) then we have:

$$\sigma_{pix,AVG}^2 = \frac{CF^2}{N_{vis}^{hires}} \frac{N_{vis}^{lores}}{N_{vis}^{hires}} \frac{1}{n_t n_\nu} \sigma_s^2, \quad (6)$$

knowing that $CF = n_t n_\nu = N_{vis}^{hires}/N_{vis}^{lores}$, after simplifications we then arrived at:

$$\sigma_{pix,AVG}^2 = \frac{CF}{N_{vis}^{hires} n_t n_\nu} \sigma_s^2 \quad (7)$$

$$= \frac{1}{N_{vis}^{hires}} \sigma_s^2 = \frac{1}{N_{vis}^{lores} n_t n_\nu} \sigma_s^2, \quad (8)$$

which is the result presented in Eq. (37), where N_{vis}^{lores} is simply the number of visibilities in the simple averaged data, i.e. $N_{vis}^{lores} = N_{vis}^{AVG}$.

This paper has been typeset from a $\text{\TeX}/\text{\LaTeX}$ file prepared by the author.